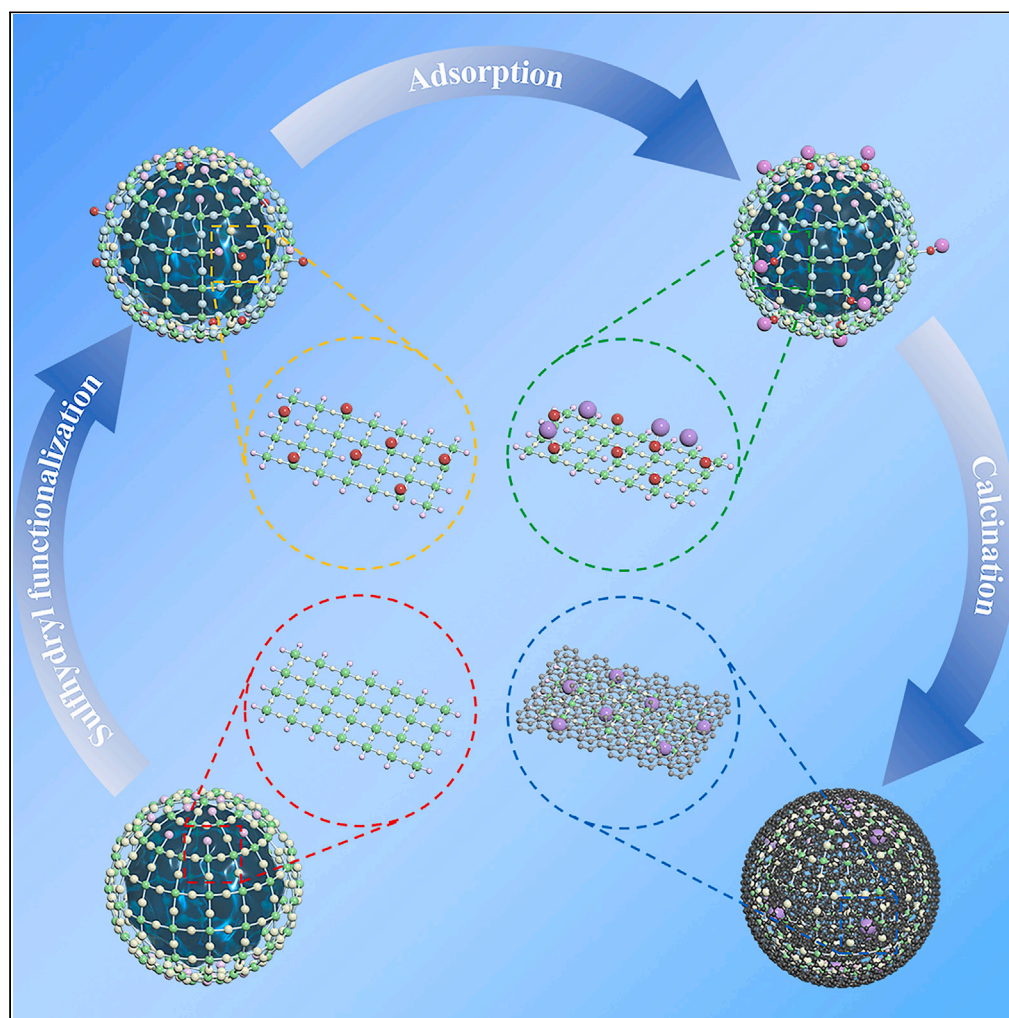## Article

Developing a novel lithium-ion battery anode material via thiol functionalization of diatom frustules plus Ag modification

Yuxin Chen, Hongchang Liu, Ze Shen, ..., Zhenyuan Nie, Hongwei Liu, Jianping Xie

hchliu2050@csu.edu.cn

Highlights

-SH active sites on diatom frustules were created by adding organic silicon sources

Thiol-functionalized diatoms plus Ag modification are used as anode material sources

DBS@C-Ag-3 anodes delivered ~660 mAh·g^{-1} after 1000 cycles at 1 A·g^{-1}

Dominant role of structure and conductivity at different temperatures was revealed

Article

Developing a novel lithium-ion battery anode material via thiol functionalization of diatom frustules plus Ag modification

Yuxin Chen,[1] Hongchang Liu,[1,2,4,*] Ze Shen,[1] Kang Yang,[1] Jinlan Xia,[1,2] Peng Yuan,[3] Zhenyuan Nie,[1,2] Hongwei Liu,[1,2] and Jianping Xie[1,2]

SUMMARY

The biosilicification of diatoms allows for the customization of the synthesis of functionalized diatom frustules. The S active sites (–SH) on diatom frustules were created by adding the organic silicon sources tetramethoxysilane (TMOS) and (3-mercaptopropyl)trimethoxysilane (MPTMS). The mechanisms of adsorption-reduction and the indirect effects of S active sites on electrochemical performance were declared. The DBS@C-Ag-3 anode material sourced from the cultivation condition with a silicon source of TMOS:MPTMS = 3:1 shows the best comprehensive performance and delivers a discharge capacity of $\sim$660 mAh·g^{-1} after 1000 cycles at 1 A·g^{-1}. The electrochemical performance of DBS@C-Ag anode materials is also found to be dominated by structure at high temperatures and conductivity at low temperatures. Such a diatom frustule structure with sulfhydryl functionalization is promising for anode materials, and it suggests a biological strategy for creating other electrode materials by modifying them with metals to improve electrochemical performances.

INTRODUCTION

Diatom biosilica (DBS) has been widely studied and applied in biosensors, drug delivery, adsorbents, and other applications due to its unique three-dimensional hollow porous structure produced by biosilicification of diatoms.[1] Recently, it has also been used as an anode material for lithium-ion batteries. Nowak et al.[2] demonstrated a discharge capacity of 400 mAh·g^{-1} after 90 cycles at 20 mA g^{-1} using *Pseudostaurosira trainorii* as a source of active materials. Norberg et al.[3] used FIB-SEM to observe a cycled diatom-based electrode; the diatom frustules were able to maintain a stable structure after cycling, which is attributed to their unique structure.

Although DBS has a natural advantage in a structure that effectively inhibits volume expansion, silica's low intrinsic conductivity is unavoidable. Carbon and metal phases can significantly improve a material's external conductivity. Nowak et al.[4] proposed using diatom biomass as a carbon precursor to create a DBS@C composite with a stable capacity of 340 mAh·g^{-1} at 100 mA g^{-1}. Wang et al.[5] used diatom biomass as a carbon precursor, significantly reduced the impedance of diatom frustules, and showed excellent performance. A chemical modification method was used in our recent work[6] to prepare diatom-based anode materials decorated with Co nanoparticles, which delivered a discharge capacity of >620 mAh·g^{-1}. However, it must be acknowledged that the cost of Co is prohibitively expensive.

In contrast, Ag is a simple conductive phase that is frequently used to improve the properties of anode materials. Jia et al.[7] created an Ag-silica-carbon composite with a capacity of 400 mAh·g^{-1}. Adsorption is a simple and efficient method for creating Ag-containing materials, particularly those with unique active sites. Yao et al.[8] achieved an ultrahigh silver adsorption capacity of 719.2 mg g^{-1} by grafting a large number of sulfhydryl (-SH) functional groups onto the surface of activated carbon. The inspiration comes from this chemical modification method of increasing the number of active sites. Diatoms, as unicellular organisms, can be cultured in different directions by changing the culture conditions. In the presence of silaffins, alkoxysilane will follow a typical sol-gel process to form a SiO$_2$ colloidal network, and the generation of synthetic silica structures *in vitro* has been reported.[9–11]

Thus, a biomodification method was used in this work to obtain thiol-functionalized diatom frustules with increased adsorption capacity. Diatoms cultured with the silicon source tetramethoxysilane (TMOS):(3-mercaptopropyl)trimethoxysilane (MPTMS) = 3:1 (3-SH) were able to achieve a balance between the degree of silica colloidal network crosslinking (DSCNC) and the degree of sulfhydryl functionalization (DSF). Diatom frustules were used to capture Ag$^+$ before making DBS@C-Ag composites. The DBS@C-Ag-3 anode prepared by 3-SH adsorbing Ag$^+$ has the best overall properties, delivering $\sim$660 mAh·g^{-1} after 1000 cycles at 1 A·g^{-1}. Furthermore, the mechanism of adsorption-reduction of S active sites, as well as the effects of structure and conductivity on Li$^+$ diffusion, was discovered.

[1]School of Minerals Processing and Bioengineering, Central South University, Changsha 410083, China
[2]Key Lab of Biometallurgy of Ministry of Education of China, Central South University, Changsha 410083, China
[3]School of Environmental Science and Engineering, Guangdong University of Technology, Guangzhou 510006, China
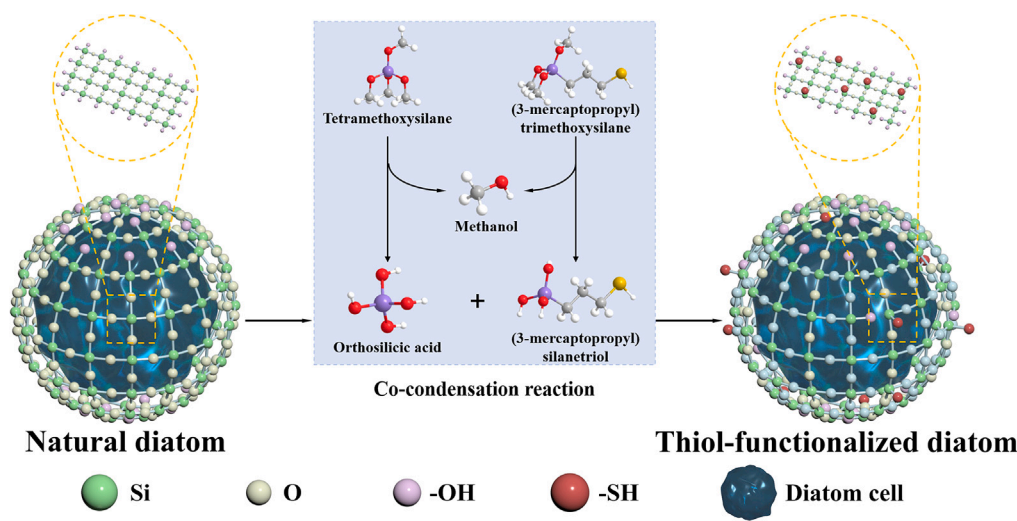[4]Lead contact
*Correspondence: hchliu2050@csu.edu.cn
https://doi.org/10.1016/j.isci.2024.108850

Figure 1. The synthesis of thiol-functionalized diatom frustules using a silica colloidal network is depicted schematically.

RESULTS AND DISCUSSION

Diatom frustule sulfhydryl functionalization

The synthesis of the silica colloidal network is depicted in Figure 1. In the culture medium, TMOS and MPTMS are hydrolyzed to form the secondary hydrolysates orthosilicic acid and (3-mercaptopropyl)silanetriol, as well as the coproduct methanol.[11] The secondary products will co-condensate in the diatom silica deposition vesicles to form a silica colloidal network containing sulfhydryl functional groups. Thiol-functionalized diatoms are produced in this manner.

Figure S1 depicts blue fluorescence images of diatom frustules cultured under various silicon source conditions using PDMPO fluorescent probes. TMOS and MPTMS can be used as alternative silicon sources to synthesize diatom frustules based on fluorescence intensity, but MPTMS inhibits diatom utilization of TMOS, which is not conducive to the synthesis of the SiO_2 colloidal network. As a result, the crosslinking and structural integrity of silica will suffer.

Figure S2 depicts the green fluorescence results of qualitative detection of -SH groups in diatom frustules. Green fluorescence is rare in natural diatoms (Figure S2A), but it can be seen in other thiol-functionalized diatoms (Figures S2B–S2D), indicating that -SH groups were successfully introduced into the diatom frustules. These sulfhydryl functional groups will serve as active sites for Ag^+ adsorption.

Thiol-functionalized diatoms were placed in $AgNO_3$ solution to adsorb Ag^+, and the -SH content of diatom frustules was determined indirectly by measuring Ag^+ adsorption capacities. Ag^+ adsorbed by 1-SH, 3-SH, and 5-SH contained 28.44, 45.09, and 39.74 mg g^{-1}, respectively. This result also reflects the side effects of the three thiol-functionalized diatom frustules.

In conclusion, because of the inhibition of MPTMS in 1-SH, the synthesis effect of the silica colloidal network is poor, as is the content of -SH introduced. However, as the use of MPTMS decreased, the DSCNC of 5-SH increased, but so did the amount of -SH that could be introduced into the frustules. Only 3-SH diatom frustules cultured with TMOS:MPTMS = 3:1 achieve a balance of DSCNC and DSF, where DSCNC determines the structure of SiO_2 and DSF affects its conductivity.

Characterization of DBS@C-Ag composites

X-ray diffraction was used to characterize the calcined DBS@C-Ag samples, and the results are shown in Figure 2A. The broad peak at 22° corresponds to the amorphous SiO_2 phase, and the peak at 24° corresponds to the carbon phase in DBS@C. The diffraction peaks for the DBS@C-Ag composites are 38.12°, 44.30°, 66.45°, 77.41°, and 81.55°, which correspond to the (111), (200), (220), (311), and (222) crystal planes of the Ag cubic crystal (JCPDS No. 01-089-3722). This suggests that after calcination, the Ag^+ adsorbed by thiol-functionalized diatoms exists as an elemental metal phase.

Thermogravimetry (TG) and inductively coupled plasma mass spectrometry (ICP-MS) were used to detect the specific components of the samples (Figure 2B). In the heating process, biosilica has no change. The increase and decrease in mass were mainly caused by C and Ag, respectively. Ag will first generate Ag_2O, which will lead to an increase in mass. However, when the temperature is higher than 300°C, Ag_2O decomposes into Ag again, and the mass decreases at this time, which means that Ag does not actually affect the results of the TG curves. Therefore, only the weight loss caused by C occurred. Then, to analyze the composition of residues, ICP-MS was used to obtain the Ag:Si molar ratio. Finally, the mass ratios of C, SiO_2, and Ag were obtained. The SiO_2 weight percentages of DBS@C-Ag-1, DBS@C-Ag-3, and DBS@C-Ag-5 were calculated to be 45.65%, 36.14%, and 35.07%, respectively (Table S1).

X-ray photoelectron spectroscopy was used to examine the chemical states of thiol-functionalized diatom (TMOS:MPTMS = 3:1) samples before adsorption (3-SH), after adsorption (3-Ag), and after calcination (DBS@C-Ag-3). Figure 3A shows that all samples contain C, N, O, and
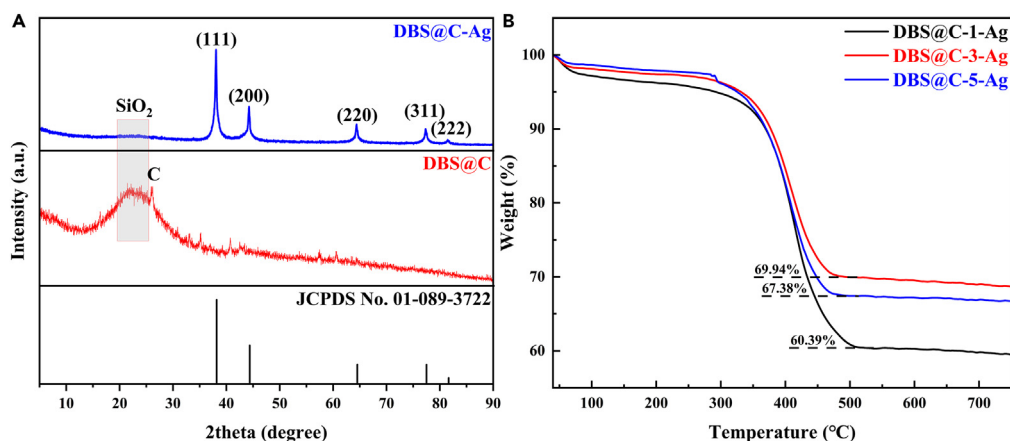
Figure 2. XRD patterns and TG curves of DBS@C-Ag composites
(A) XRD patterns and (B) TG curves.

Si, but there is no Ag in the 3-SH sample prior to adsorption, whereas Ag is present in 3-Ag and DBS@C-Ag-3, indicating that the 3-SH sample successfully captured Ag^+. This corresponds to the experimental expectation. S is present in both the 3-SH and 3-Ag samples but not in the DBS@C-Ag-3 sample.

The positions of the C–C (284.8 eV) peaks, C=N/C–O (286.2 eV) peaks, C–N/C=O (287.5/287.7 eV) peaks, and O–C=O (288.3/288.5 eV) peaks belonging to the 3-SH and 3-Ag samples are close, indicating that the organic composition of the diatom cell does not change significantly before and after adsorption. However, in the DBS@C-Ag-3 sample, the C–C and C=N/C–O peaks are weakened, indicating that the organic matter containing this type of bonding is the main component of pyrolysis (Figure 3B).

From Figure 3C, the N 1s spectra of the 3-SH and 3-Ag samples show almost no difference. The N 1s spectrum can be divided into three types of peaks with –NH_2 (399.8 eV), N–O (401.0 eV), and –NH_4^+ (402.2 eV), which are derived from organic matter, such as protein. After calcination, the N 1s spectrum can be deconvoluted into pyrrolic-N (398.4 eV), pyridinic-N (399.6 eV), and graphitic-N (400.9 eV).[12] These results demonstrate the successful incorporation of nitrogen atoms from the carbonization of nitrogen-containing biomass in diatoms into the carbon framework. Pyrrolic-N and pyridinic-N are beneficial to lithium storage and improve capacity, and graphitic-N is beneficial to electron transfer and improves electrical conductivity.[13,14] The electronegativity of the N atom (χ_N = 3.04) is stronger than that of the C atom (χ_C = 2.55), which can enhance the adsorption of Li^+ and further improve the performance of lithium storage. The O 1s spectrum can be deconvoluted into O–H (531.6 eV), Si–O (532.5 eV) and organic C–O (534 eV) (Figure 3D).

Deconvolution of the S 2p spectrum of 3-SH (Figure 3E) reveals the presence of an S 2$p_{3/2}$ peak (163.3 eV), an S 2p peak (164.4 eV), an $SO_4^{2-}/S_2O_3^{2-}$ peak (168.2 eV), and an extra satellite (Sat.) peak (169.2 eV). The S 2$p_{3/2}$ peak is associated with -SH, while the other two S element peaks can be regarded as invalid S active sites. The S peak associated with the –SH of 3-SH shifts to the $-S^{-1}$ peak (162.8 eV) in the 3-Ag sample, which is attributed to Ag^+ adsorption. The S peaks disappear after calcination, which is attributed to high-temperature pyrolysis and indicates that the S active sites in the diatom frustules will affect the electrochemical performance of the DBS@C-Ag anodes indirectly through the adsorption capacity of Ag^+ (conductivity) rather than directly participating in the electrochemical process.

Except for the 3-SH samples devoid of Ag, the peaks at 368.3 and 374.3 eV in the 3-Ag sample correspond to Ag^0 and Ag 3$d_{3/2}$, respectively, indicating that Ag^+ is reduced by –SH, causing it to exist in the form of elemental Ag and be retained during calcination (Figure 3F). Adsorption and reduction processes are proposed (Equation 1) based on the aforementioned analysis results, and the diagram is shown in Figure 4.

$$- SH + Ag^+ \rightarrow\ - S^- + H^+ + Ag^+ \rightarrow\ - S - Ag + H^+ \qquad \text{(Equation 1)}$$
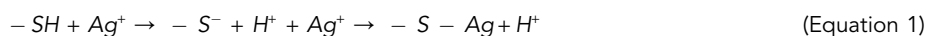
SEM-energy dispersive spectroscopy (EDS) was used to characterize the 3-SH, 3-Ag, and DBS@C-Ag-3 samples (Figure S3). The EDS results of all samples, similar to the previous analysis, show a uniform distribution of C, O, and Si elements in the diatom frustules. The atomic ratio of S in the 3-Ag sample is 0% (Figure S3B), which is probably due to masking of the S signal by Ag nanoparticles (Ag NPs) obtained by reduction.

Transmission electron microscopy (TEM)-energy dispersive X-ray spectroscopy was used to characterize the morphology and structure of DBS@C-Ag-3, and the results are shown in Figures 5 and S4. The overall image of DBS@C-Ag-3 is shown in Figure 5A. By gradually increasing the size of the diatom frustule, it is discovered that there are a large number of particles on its surface, the size of which is approximately 10 nm (Figures 5B and 5C). Figure 5D depicts the lattice stripes of DBS@C-Ag-3 samples under high-resolution TEM (HRTEM). The crystal plane spacing at position I is 2.038 Å after calibration, corresponding to the (200) plane of the Ag cubic crystal. The crystal plane spacing at position II is 2.356 Å, which corresponds to the Ag cubic crystal's (111) plane. The HRTEM image of the carbon
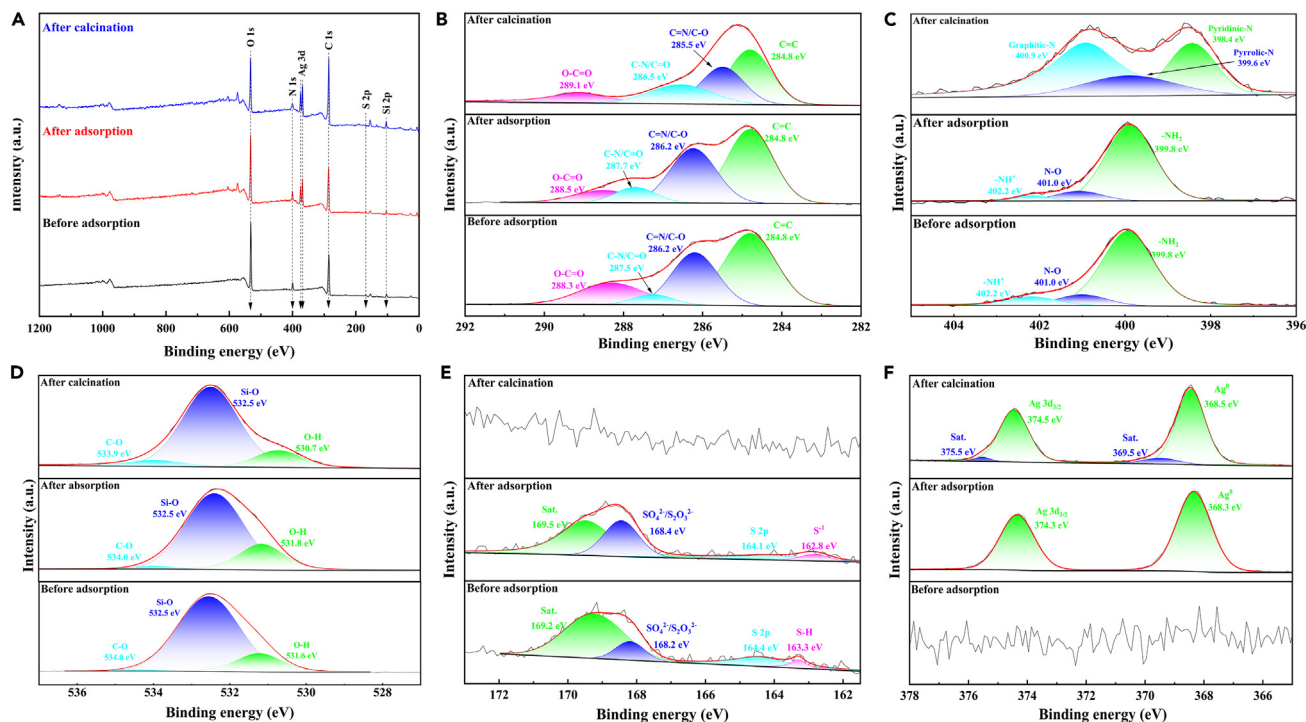
Figure 3. XPS spectra and fitted results of 3-SH, 3-Ag, and DBS@C-Ag-3
(A) Survey, (B) C 1*s*, (C) N 1*s*, (D) O 1*s*, (E) S 2*p*, and (F) Ag 3*d*.

layer shows that the carbon layer is amorphous (Figure S5). The results tested in our previous work show that it is mainly composed of hard carbon, which is related to the fact that its precursors are biological organic matter.[6] The SAED image of the DBS@C-Ag-3 sample is shown in Figure 5E. The concentric diffraction rings, which correspond to the crystal planes of Ag cubic crystals from inside to outside, demonstrate the polycrystalline properties of Ag NPs. Figure S5 depicts the element distribution in DBS@C-Ag-3 samples. The elements C, O, and Si are uniformly distributed, Ag is granular, and S is eliminated after calcination, which is similar to the EDS result in Figure S3C but difficult to see.

Electrochemical performance

Half-cells were assembled with lithium sheets as the counter electrode and reference electrode to investigate the electrochemical performance of the DBS@C-Ag anodes. The first four CV curves of the DBS@C and DBS@C-Ag-3 anodes are shown in Figure 6. The first CV curve of the DBS@C anode includes 4 reduction peaks at 2.30, 1.15, 0.25, and 0.01 V, which are attributed to the decomposition of the electrolyte, the formation of the solid electrolyte interface (SEI) phase, the reduction of SiO_2 ($SiO_2 + 4Li^+ + 4e^- \rightarrow 2Li_2O + Si$; $2SiO_2 + 4Li^+ + 4e^- \rightarrow Li_4SiO_4 + Si$; $5SiO_2 + 4Li^+ + 4e^- \leftrightarrow 2Li_2Si_2O_5 + Si$), and the alloying reaction of Si ($Si + xLi^+ + xe^- \leftrightarrow Li_xSi$), respectively[15,16]; and 2 oxidation peaks at 0.40 and 0.97 V are attributed to the formation of silicon nanoclusters and the dealloying reaction of Li_xSi ($Li_xSi \leftrightarrow Si + xLi^+ + xe^-$), respectively. The peaks of electrolyte decomposition, SEI layer formation, and SiO_2 reduction gradually disappear in subsequent cycles, and the curves gradually overlap, indicating the reversibility of the lithiation reaction (Figure 6A). The CV result of DBS@C-Ag-3 is nearly identical to that of DBS@C (Figure 6B), as are the CV results of the DBS@C-Ag-1 and DBS@C-Ag-5 anodes (Figure S6). According to their CV results, SEI layer formation and SiO_2 reduction are the main contributors to the initial irreversible capacity, resulting in a low initial Coulombic efficiency (ICE).

The lithium storage mechanism of DBS@C-Ag electrodes was also analyzed by CV curves. The electrochemical behavior can be expressed by Equations 2 and 3, where *i*, *v*, *a*, and *b* are the current, the scan rate, and arbitrary coefficients, respectively. When b is equal to 0.5, the electrochemical system is controlled by ionic diffusion, whereas an a-value of 1 indicates that the system is controlled by the pseudocapacitive effect. Figure 7 shows that the b_C values of the reduction reaction of DBS@C-Ag electrodes are 0.54, 0.52, and 0.58, indicating that the reduction reaction is controlled by diffusion. It is worth noting that the b_A values of the oxidation reaction are 0.94, 0.71, and 0.73, respectively, indicating that the delithiation process of DBS@C-Ag-1 is almost completely controlled by pseudocapacitance, while the results of the other two electrodes are similar and are still dominated by ion diffusion. This may be related to the inhibition of the synthesis of 1-SH frustules by MPTMS, resulting in more silica structural vacancies that are not conducive to the mass transfer process.
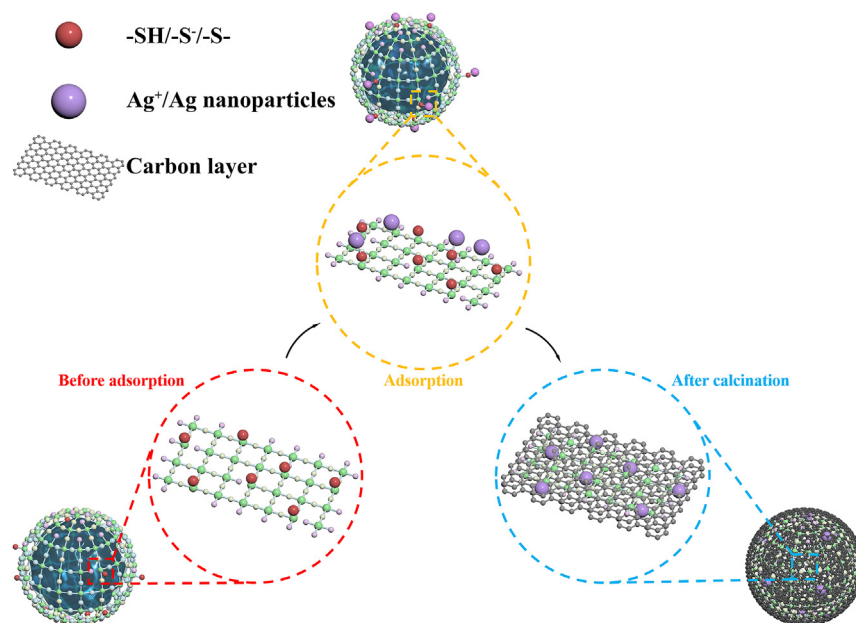
Figure 4. The conversion diagram of S active sites and Ag.

$$i = av^b \qquad \text{(Equation 2)}$$

$$\log i = \log a + b \log v \qquad \text{(Equation 3)}$$

$$i_v = k_1 v + k_2 v^{1/2} = av^b \qquad \text{(Equation 4)}$$

Moreover, Equation 4 was employed to determine the contribution of the capacitive and diffusion-controlled capacity. In Equation 4, i_v is the current response at a specific voltage, embracing $k_1 v$ (capacitive contribution) and $k_2 v^{1/2}$ (diffusion-controlled contribution). Overall, the electrochemical behavior of DBS@C-Ag electrodes is mainly the diffusion behavior of Li$^+$. With increasing scanning rate, the behavior of the capacitors becomes more prominent. However, the strange thing is that, although the b_A value of DBS is 0.94, its pseudocapacitance contribution rate is not much different from that of the other two. A reasonable speculation is the limitation of the reduction reaction of biosilica on the Li$^+$ released from the dealloying reaction.

A galvanostatic charge-discharge test was used to investigate the long-term cycle performance of DBS@C-Ag anodes (Figure 8A). DBS@C-Ag-1, DBS@C-Ag-3, and DBS@C-Ag-5 have initial discharge capacities and Coulombic efficiencies of 1434.33 mAh·g^{-1} and 23.18%, 1324.12 mAh·g^{-1} and 30.68%, and 1257.80 mAh·g^{-1} and 26.20%, respectively, at 100 mA g^{-1}. Ag NPs have a positive effect on ICE when compared to the DBS@C anode (ICE = 19.43%) (Figure S7). However, the ICE of DBS@C-Ag anodes remains low, which is consistent with the CV results and can be improved through prelithiation. The discharge capacity and capacity retention of the DBS@C-Ag-1, DBS@C-Ag-3, and DBS@C-Ag-5 anodes after 300 cycles are 423.37 mAh·g^{-1} and 29.52%, 657.25 mAh·g^{-1} and 49.64%, and 565.49 mAh·g^{-1} and 44.96%, respectively. All of the Coulombic efficiencies are consistent at >99%. Furthermore, the discharge capacities of DBS@C-Ag anodes are increasing, which is attributed to active material activation[17,18] and the improvement of electrical conductivity to SiO$_2$ by Ag NPs. As a result, the DBS@C-Ag-3 anode with the highest Ag content performs the best in terms of cycle performance. By applying a potentiostatic step (2 mV vs. Li/Li$^+$ for 48 h)[3] to accelerate the activation of SiO$_2$, the ICE increases to 97.04%, and the DBS@C-Ag-3 anode delivers a stable discharge capacity of ~620 mAh·g^{-1} after 200 cycles (Figure S8).

The DBS@C-Ag-3 anode has the best rate performance (Figure 8B), which is consistent with the results of the long-term cycle performance. The DBS@C-Ag-3 discharge capacities are 437.94, 380.37, 315.58, 276.56, 239.19, 190.20, and 155.73 mAh·g^{-1} at current densities of 0.1, 0.2, 0.5, 1, 2, 5, and 10 A·g^{-1}, respectively. When the current density returns to 100 mA g^{-1}, the discharge capacity is 512.92 mAh·g^{-1}, indicating that the DBS@C-Ag-3 anode has good stability and that a higher current density has an accelerating effect on anode active material activation. At high rates, all of the DBS@C-Ag anodes exhibit excellent cycle stability and high Coulombic efficiency (>99%). When the current density reaches 10 A·g^{-1}, the Coulombic efficiency fluctuates, indicating structural instability at this current density. Figure 8C depicts the long-term cycle performance of the DBS@C-Ag-3 anode at 1 A·g^{-1}. The capacity of DBS@C-Ag-3 stops increasing until the 775th cycle, when it delivers a stable capacity of 660 mAh·g^{-1}. Considering the weight percentage of SiO$_2$ in the DBS@C-Ag-3 composite (36.14%), the reversible capacity of SiO$_2$ can reach >1800 mAh·g^{-1}. The capacity retention increases from 31.99% to 105.23% (the initial discharge capacity is 627.22 mAh·g^{-1}). This demonstrates that anode active materials are completely activated after a long period of time. Of note, the cycle
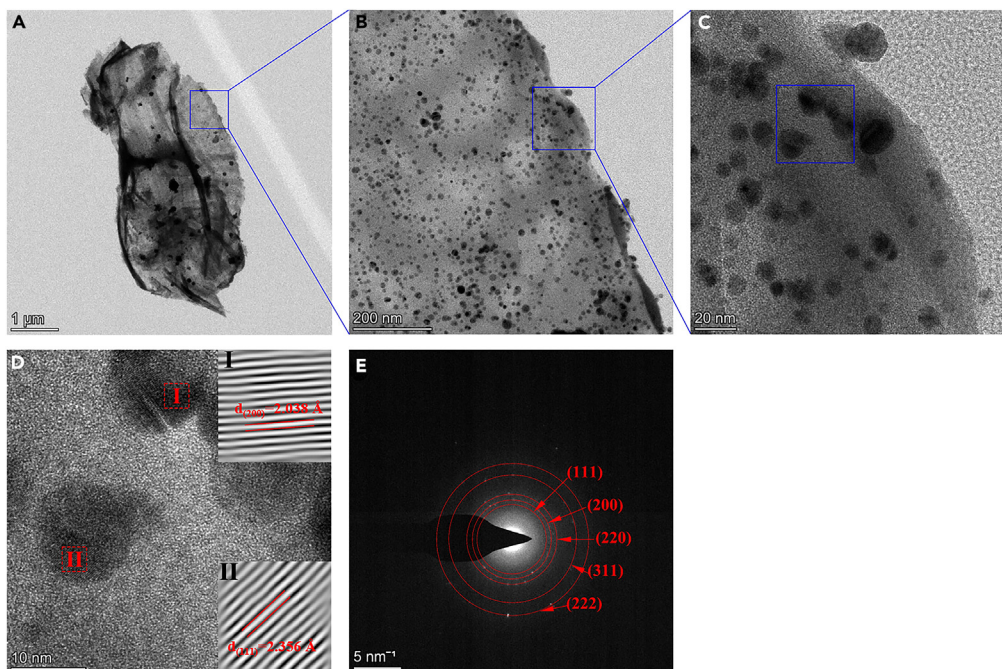
Figure 5. Morphology and structure of DBS@C-Ag-3

(A–D) TEM images and (E) SAED image. The scale bars are (A) 1 μm, (B) 200 nm, (C) 20 nm, (D) 10 nm, and (E) 5 nm^{-1}.

performances of all DBS@C-Ag anodes initially decrease and then increase slowly. This phenomenon is common, especially in metal oxide anodes, and the potential mechanism has also been clarified.[19,20] Due to the poor conductivity of SiO_2, the lithiation reaction initially took place only on the surface and was not activated internally. Subsequently, a new fast electron transport path (lithiation product) is generated, which improves the conductivity and increases the contribution capacity of the reversible reaction, thus forming the phenomenon that the capacities decrease at first and then increase.

Electrochemical impedance spectroscopy (EIS) was performed in the frequency range of 0.01–100 kHz to investigate the effect of Ag NPs on the electrical conductivity of diatom frustules (Figure 9A). The sample charge transfer impedance (R_{ct}) is related to the Ag$^+$ adsorption capacity, and the DBS@C-Ag-3 anode has the lowest R_{ct} value of 225.10 Ω (2000 Ω of the DBS@C anode, Figure S9). The conductivity of diatom frustules is significantly improved by Ag NPs. The diffusion coefficient of lithium ions (D_{Li^+}) is calculated using the following equation using the EIS curves[21]:

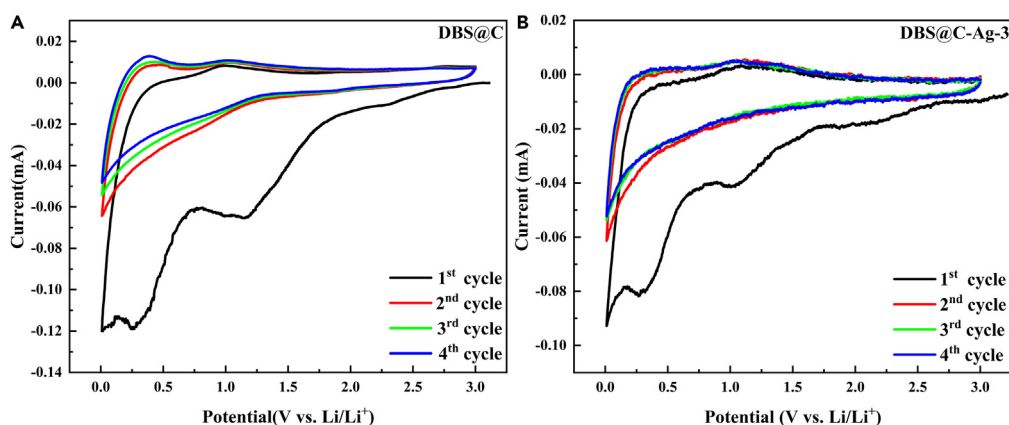$$D = R^2 T^2 / 2A^2 n^4 F^4 C^2 \sigma^2 \qquad \text{(Equation 5)}$$

Figure 6. CV curves of DBS@C and DBS@C-Ag-3 anodes
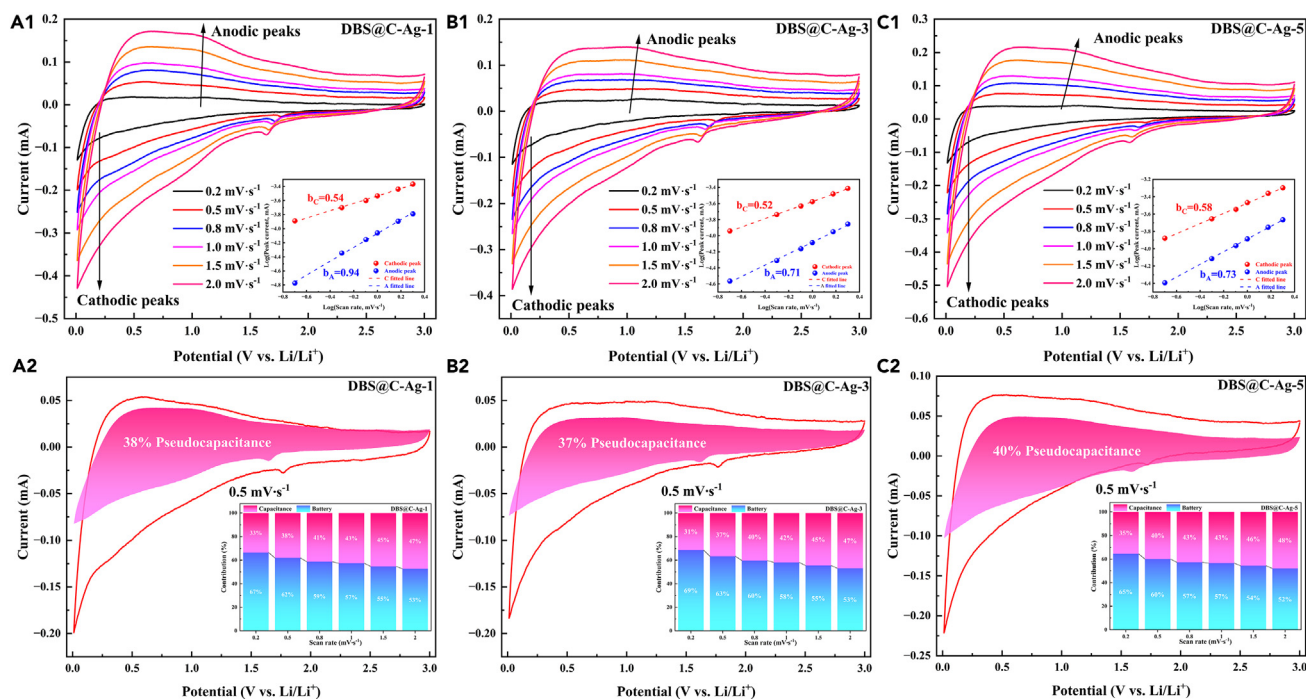
(A) DBS@C and (B) DBS@C-Ag-3.

Figure 7. Pseudocapacitance contribution of DBS@C-Ag anodes
(A1, A2) DBS@C-Ag-1, (B1, B2) DBS@C-Ag-3, and (C1, C2) DBS@C-Ag-5.

where R is the gas constant, T is the absolute temperature, A is the electrode surface area, n is the number of electrons per molecule during oxidation, F is the Faraday constant, C is the Li^+ concentration, and σ is the Warburg factor (Figure 9B). Table S2 displays the calculated results and EIS result parameters. DBS@C-Ag-1, DBS@C-Ag-3, and DBS@C-Ag-5 have D_{Li^+} values of 1.62×10^{-16}, 5.39×10^{-16}, and 5.54×10^{-16} $cm^2\ s^{-1}$, respectively.

The improvement in electrical conductivity is beneficial to the diffusion of Li^+ in the bulk phase. However, DBS@C-Ag-5 has a higher D_{Li^+} than DBS@C-Ag-3 in the DBS@C-Ag anodes. The only difference between them, aside from conductivity, is the structure. As previously stated, in 1-SH, 3-SH, and 5-SH diatoms, 1-SH causes a poor DSCNC due to MPTMS inhibition, resulting in a low DSF. The DSCNC of 5-SH was the best, but the sulfhydryl content decreased as the MPTMS content decreased. Only 3-SH manages to strike a balance between the DSCNC and DSF. According to the EIS results, the structure appears to be a more important factor influencing the diffusion of Li^+ in the SiO_2 phase than conductivity. Furthermore, the D_{Li^+} values of DBS@C-Ag-3 and DBS@C-Ag-5 are close, indicating that the negative effect of the low DSCNC on Li^+ diffusion can be balanced by the positive effect of DSF on improving conductivity by adsorbing Ag^+.

Temperature, in addition to conductivity, also has a significant impact on electrode performance. As the temperature rises, the diffusion of Li^+ accelerates, resulting in a higher capacity electrode. Thus, constant current charge-discharge tests of DBS@C-Ag-3 and DBS@C-Ag-5 anodes at different temperatures are performed to further evaluate the effect of the structure (Figure 10). At 50°C and 60°C, it is clear that the DBS@C-Ag-5 anode has a higher discharge capacity and outperforms the DBS@C-Ag-3 anode (Figure 10A). Here, the role of electrical conductivity seems to be ignored. It has also been confirmed in previous studies that with increasing temperature, electrical conductivity is no longer a factor affecting the electrochemical performance of silica anode materials.[19] Furthermore, Figures 10B and 10C show that the charge-discharge platform at 0.25 V becomes more visible with increasing temperature, indicating an improvement in reaction kinetics. This result emphasizes the significance of structural integrity in the diffusion of Li^+ at high temperatures. In contrast, at lower temperatures, Li^+ diffusion is less intense, and conductivity will dominate the electrochemical performance of the electrode.

In conclusion, thiol-functionalized diatoms capable of capturing Ag^+ were obtained through biological modification and used to create DBS@C-Ag anode materials. DSCNC and DSF determined the structure of SiO_2 and anode material conductivity, respectively. The S active site adsorption-reduction mechanism was discovered. The DBS@C-Ag-3 anode balanced the DSCNC and DSF and had the best overall performance, with a discharge capacity of ~660 mAh·g^{-1} at 1 A·g^{-1} after 1000 cycles. Furthermore, charge-discharge tests at various temperatures reveal that the electrochemical performance of DBS@C-Ag anodes is primarily influenced by structure at high temperatures and conductivity at low temperatures. The biological strategy of controlling the synthesis of thiol-functionalized diatom frustules appears promising for the fabrication of anode materials with improved electrochemical performance.
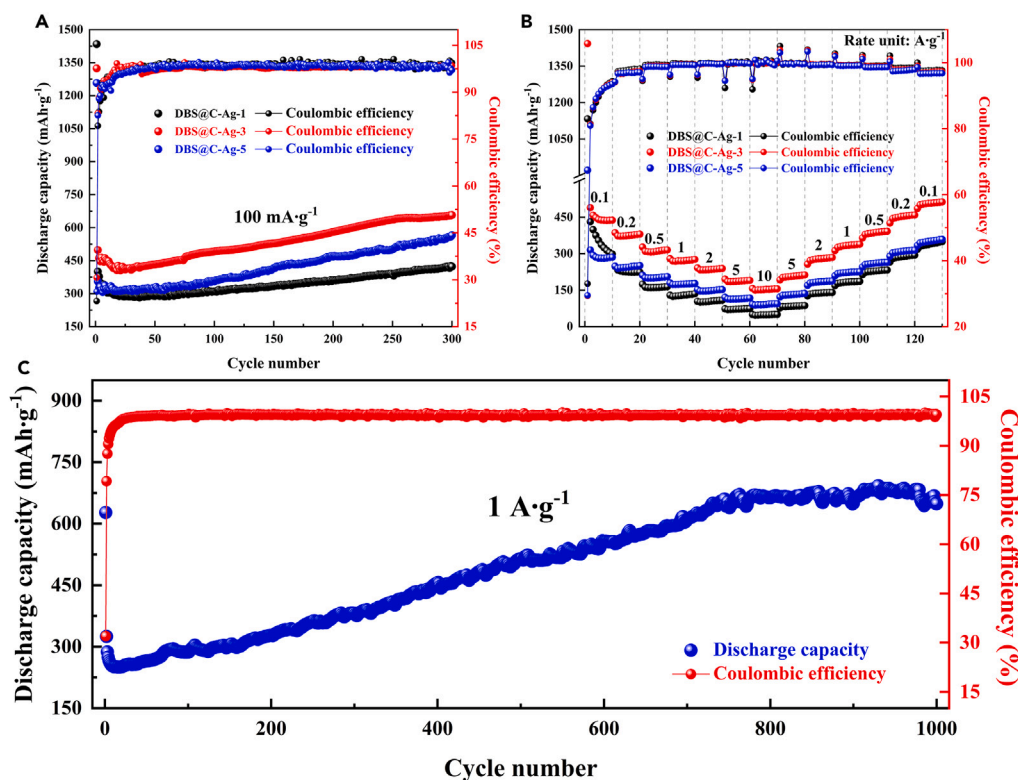
Figure 8. Cycle and rate performances of DBS@C-Ag anodes
(A) DBS@C-Ag anode long-term cycle performance at 100 mA g^{-1}, (B) DBS@C-Ag anode rate performance, and (C) DBS@C-Ag-3 anode high-rate (1 A·g^{-1}) cycle performance.

Limitations of the study

The limitation of this study is that the Coulombic efficiency is still low in the initial few cycles for the DBS anode and the activation term is too long. Therefore, it is still necessary to carry out more modification and prelithiation experiments to increase the initial Coulombic efficiency in the future.

STAR★METHODS

Detailed methods are provided in the online version of this paper and include the following:

- KEY RESOURCES TABLE
- RESOURCE AVAILABILITY
  - Lead contact
  - Materials availability
  - Data and code availability
- EXPERIMENTAL MODEL AND STUDY PARTICIPANT DETAILS
- METHOD DETAILS
  - Diatom culture
  - Fluorescence detection of diatom frustule synthesis
  - Fluorescence detection of thiol moieties
  - Preparation of DBS@C-Ag composites
  - Materials characterization
  - Half-cell assembly
  - Electrochemical performance testing
- QUANTIFICATION AND STATISTICAL ANALYSIS

SUPPLEMENTAL INFORMATION
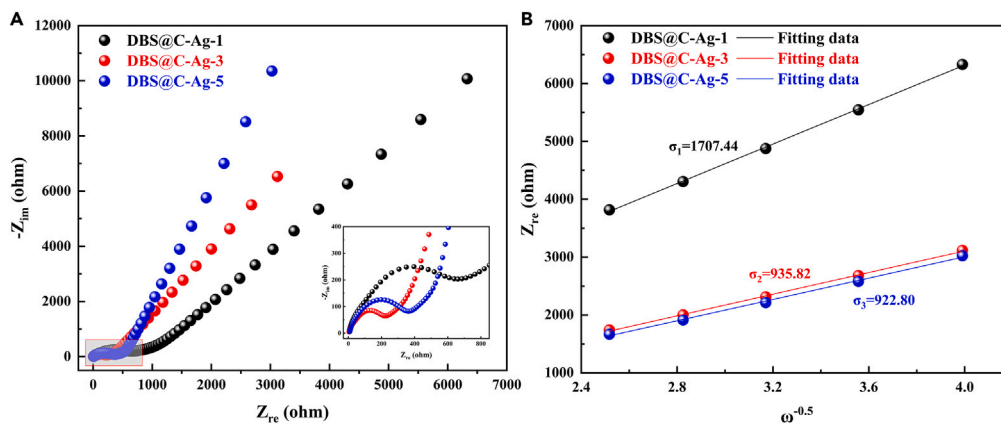
Supplemental information can be found online at https://doi.org/10.1016/j.isci.2024.108850.

Figure 9. EIS plots and Warburg factors of DBS@C-Ag anodes
(A) EIS plots and (B) Warburg factors.

AUTHOR CONTRIBUTIONS

Conceptualization, Hongchang Liu, J. Xia, and P.Y.; methodology, Hongchang Liu, Z.N., Hongwei Liu, and J. Xie; investigation, Y.C., Z.S., K.Y., and Z.N.; writing – original draft, Y.C. and Hongchang Liu; writing – review & editing, Hongchang Liu, J. Xia, and P.Y.; funding acquisition, Hongchang Liu and J. Xia; resources, Hongchang Liu, Hongwei Liu, and J. Xie; supervision, Hongchang Liu.
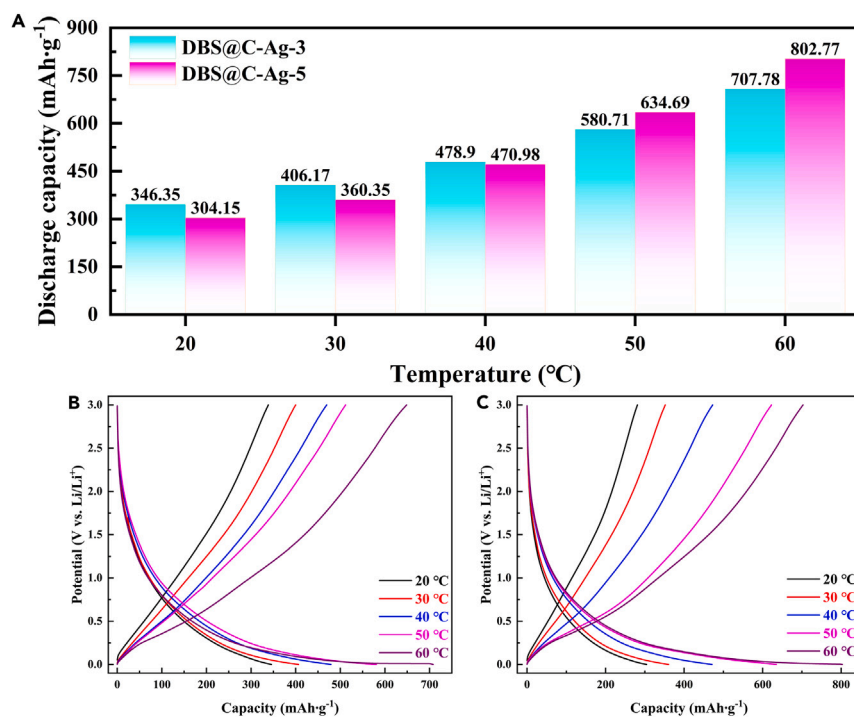
Figure 10. Discharge capacities and charge-discharge capacity curves of DBS@C-Ag anodes
(A) Discharge capacities of DBS@C-Ag-3 and DBS@C-Ag-5 anodes, and (B) DBS@C-Ag-3 and (C) DBS@C-Ag-5 charge-discharge capacity curves at temperatures of 20°C, 30°C, 40°C, 50°C, and 60°C.

DECLARATION OF INTERESTS

The authors declare no competing interests.

REFERENCES

1. Sun, X.W., Zhang, Y.X., and Losic, D. (2017). Diatom silica, an emerging biomaterial for energy conversion and storage. J. Mater. Chem. A 5, 8847–8859.

2. Nowak, A.P., Sprynskyy, M., Brzozowska, W., and Lisowska-Oleksiak, A. (2019). Electrochemical behavior of a composite material containing 3D-structured diatom biosilica. Algal Res. 41, 101538.

3. Norberg, A.N., Wagner, N.P., Kaland, H., Vullum-Bruer, F., and Svensson, A.M. (2019). Silica from diatom frustules as anode material for Li-ion batteries. RSC Adv. 9, 41228–41239.

4. Nowak, A.P., Sprynskyy, M., Wojtczak, I., Trzciński, K., Wysocka, J., Szkoda, M., Buszewski, B., and Lisowska-Oleksiak, A. (2020). Diatoms Biomass as a Joint Source of Biosilica and Carbon for Lithium-Ion Battery Anodes. Materials 13, 1673.

5. Wang, Z., Zhao, J., Liu, S., Cui, F., Luo, J., Wang, Y., Zhang, S., Zhang, C., Yang, X., and Yang, X.J. (2021). Cultured diatoms suitable for the advanced anode of lithium ion batteries. ACS Sustainable Chem. Eng. 9, 844–852.

6. Chen, Y.X., Liu, H.C., Xie, W.Q., Shen, Z., Xia, J.L., Nie, Z.Y., and Xie, J.P. (2023). Diatom Frustules Decorated with Co Nanoparticles for the Advanced Anode of Li-Ion Batteries. Small 19, 2300707.

7. Jia, D., Wang, K., and Huang, J. (2017). Filter paper derived nanofibrous silica–carbon composite as anodic material with enhanced lithium storage performance. Chem. Eng. J. 317, 673–686.

8. Yao, Z., Shao, P., Fang, D., Shao, J., Li, D., Liu, L., Huang, Y., Yu, Z., Yang, L., Yu, K., and Luo, X. (2022). Thiol-rich, porous carbon for the efficient capture of silver: Understanding the relationship between the surface groups and transformation pathways of silver. Chem. Eng. J. 427, 131470.

9. Marner, W.D., Shaikh, A.S., Muller, S.J., and Keasling, J.D. (2008). Morphology of Artificial Silica Matrices Formed via Autosilification of a Silaffin/Protein Polymer Chimera. Biomacromolecules 9, 1–5.

10. Selvaraj, V., Thomas, N., Anthuvan, A.J., Nagamony, P., and Chinnuswamy, V. (2018). Amine-functionalized diatom frustules: a platform for specific and sensitive detection of nitroaromatic explosive derivative. Environ. Sci. Pollut. Res. Int. 25, 20540–20549.

11. Lang, Y., del Monte, F., Collins, L., Rodriguez, B.J., Thompson, K., Dockery, P., Finn, D.P., and Pandit, A. (2013). Functionalization of the living diatom Thalassiosira weissflogii with thiol moieties. Nat. Commun. 4, 3683.

12. Sheng, Z.H., Shao, L., Chen, J.J., Bao, W.J., Wang, F.B., and Xia, X.H. (2011). Catalyst-free synthesis of nitrogen-doped graphene via thermal annealing graphite oxide with melamine and its excellent electrocatalysis. ACS Nano 5, 4350–4358.

13. Ma, C., Shao, X., and Cao, D. (2012). Nitrogen-doped graphene nanosheets as anode materials for lithium ion batteries: a first-principles study. J. Mater. Chem. 22, 8911–8915.

14. Cai, D., Wang, S., Lian, P., Zhu, X., Li, D., Yang, W., and Wang, H. (2013). Superhigh capacity and rate capability of high-level nitrogen-doped graphene sheets as anode materials for lithium-ion batteries. Electrochim. Acta 90, 492–497.

15. Chang, W.S., Park, C.M., Kim, J.H., Kim, Y.U., Jeong, G., and Sohn, H.J. (2012). Quartz (SiO$_2$): a new energy storage anode material for Li-ion batteries. Energy Environ. Sci. 5, 6895–6899.

16. Sun, Q., Zhang, B., and Fu, Z.W. (2008). Lithium electrochemistry of SiO$_2$ thin film electrode for lithium-ion batteries. Appl. Surf. Sci. 254, 3774–3779.

17. Shen, Y., Cao, Z., Wu, Y., Cheng, Y., Xue, H., Zou, Y., Liu, G., Yin, D., Cavallo, L., Wang, L., and Ming, J. (2020). Catalysis of silica-based anode (de-)lithiation: compositional design within a hollow structure for accelerated conversion reaction kinetics. J. Mater. Chem. A 8, 12306–12313.

18. Liu, T., Qu, Y., Liu, J., Zhang, L., Cheng, B., and Yu, J. (2021). Core-Shell Structured C@SiO$_2$ Hollow Spheres Decorated with Nickel Nanoparticles as Anode Materials for Lithium-Ion Batteries. Small 17, 2103673.

19. Entwistle, J.E., Booth, S.G., Keeble, D.S., Ayub, F., Yan, M., Corr, S.A., Cumming, D.J., and Patwardhan, S.V. (2020). Insights into the Electrochemical Reduction Products and Processes in Silica Anodes for Next-Generation Lithium-Ion Batteries. Adv. Energy Mater. 10, 2001826.

20. Chen, Y., Liu, H., Yang, K., Nie, Z., Xia, J., Shen, Z., Xie, J., and Liu, H. (2023). Insights into a crystallization-like activation mechanism of diatom biosilica as an anode for next-generation Li-ion batteries. J. Mater. Chem. A 11, 16704–16713.

21. Tang, C., Liu, Y., Xu, C., Zhu, J., Wei, X., Zhou, L., He, L., Yang, W., and Mai, L. (2018). Ultrafine Nickel-Nanoparticle-Enabled SiO$_2$ Hierarchical Hollow Spheres for High-Performance Lithium Storage. Adv. Funct. Mater. 28, 1704561.

STAR★METHODS

KEY RESOURCES TABLE

REAGENT or RESOURCE	SOURCE	IDENTIFIER
Biological samples		
Navicula sp.	Freshwater Algae Culture Collection at the Institute of Hydrobiology, China	FACHB-2515
Chemicals, peptides, and recombinant proteins		
Sodium metasilicate	Sigma-Aldrich	S4392
TMOS	Macklin	T819504
MPTMS	Macklin	M812736
PDMPO	Yeasen	40768ES50
7-Fluorobenzofuran-4-sulfonate ammonium	Acmec	F38320
Boric acid	Macklin	B802844
EDTA	Macklin	E870289
Silver nitrate	Aladdin	S433969
Carbon black	Canrd	MA-EN-CO-010212
PVDF	Canrd	MA-EN-BI-01030P
N-methyl-2- 354pyrrolidine	Canrd	MA-EN-OT-01011A
Electrolyte: 1 M $LiPF_6$ in EC: DEC: EMC = 1:1:1	Canrd	MA-EN-EL-0U0116
Software and algorithms		
Adobe Photoshop	Adobe	https://www.adobe.com/products/photoshop.html
Origin 2023	OriginLab	https://www.originlab.com/index.aspx?go=Products/Origin
DigitalMicrograph	Gatan	https://www.gatan.com/products/tem-analysis/digitalmicrograph-software
3Ds Max	Autodesk	https://www.autodesk.com.cn/products/3ds-max/overview?term=1-YEAR&tab=subscription
XPSPEAK 4.1	XPSPEAK	https://xpspeak.software.informer.com/4.1/

RESOURCE AVAILABILITY

Lead contact
Further information and requests for resources and reagents should be directed to and will be fulfilled by the lead contact, Hongchang Liu (hchliu2050@csu.edu.cn).

Materials availability
This study did not generate new unique reagents.

Data and code availability
(1) All data reported in this paper will be shared by the lead contact upon request.
(2) This paper does not report any original code.
(3) Any additional information required to reanalyze the data reported in this paper is available from the lead contact upon request.

EXPERIMENTAL MODEL AND STUDY PARTICIPANT DETAILS

This study does not use experimental models typical in the life sciences.

METHOD DETAILS

Diatom culture

The diatom seed (*Navicula* sp.) was purchased from the Freshwater Algae Culture Collection at the Institute of Hydrobiology in Wuhan, China, and cultured in the laboratory. The initial cell density in the culture was 10^6 cells·mL^{-1}. A customized flume (50 cm $\times$ 27 cm $\times$ 30 cm) was placed in the light incubator as the diatom culture device. The culture conditions included a 12 h:12 h light-dark time ratio, a light intensity of 2300 lx, aeration, and a constant temperature of 23°C. Diatoms were cultured in f/2 medium in artificial sea water. To culture thiol-functionalized diatoms, the silicon source (Na$_2$SiO$_3$·9H$_2$O) was replaced by a mixed solution of TMOS and MPTMS with the same concentration of Si. The TMOS/MPTMS mixed ratios were 1:1, 3:1, and 5:1, and the thiol-functionalized diatoms were designated 1-SH, 3-SH, and 5-SH, respectively.

Fluorescence detection of diatom frustule synthesis

The diatom growth activity in the presence of TMOS and MPTMS was determined using the LysoSensor lysosome yellow/blue fluorescent probe [2-(4-pyridyl)-5-(4-(2-dimethylaminoethylaminocarbamoyl)methoxy)phenyl)oxazole] (PDMPO). Before obtaining the cultured diatoms, a 10 mL diatom solution was taken and PDMPO was added. Diatoms stained with frustules were obtained after 24 h of starvation culture by washing with deionized water. The specimens were imaged with a fluorescence microscope (Nexcope NE900) equipped with a λ = 405 nm (blue-violet) laser to produce blue fluorescence, which can reflect diatom valve synthesis during cultivation.

Fluorescence detection of thiol moieties

Thiol moieties in diatom frustules were fluorescently labeled by incubating cleaned frustules in sulfhydryl staining solution, which was prepared in 0.1 M boric acid buffer containing 1 mM EDTA (pH 9.5), and 5 mg of 7-fluorobenzofuran-4-sulfonate ammonium salt was added. The diatoms were then dispersed in 5 mL of staining solution before being incubated for 1 h and washed 23 times with deionized water. To produce green fluorescence, the specimens were imaged with a λ = 510 nm (green) laser.

Preparation of DBS@C-Ag composites

DBS@C-Ag composites were prepared by collecting cultured diatoms, washing them with 1 M HCl and absolute ethanol, and then freeze-drying them to obtain dried diatom powder. To adsorb Ag$^+$, 0.25 g of 1-SH, 3-SH, and 5-SH diatom powders were added to 100 mL of 0.1 M AgNO$_3$ solution, stirred for 30 min, and centrifuged to dry. Likewise, the dried powders were designated 1-Ag, 3-Ag, and 5-Ag. Finally, the adsorbed products were calcined for 3 h in an Ar atmosphere at 600 °C at a heating rate of 5 °C min^{-1}. DBS@C-Ag-1, DBS@C-Ag-3, and DBS@C-Ag-5 were the final products obtained. Furthermore, DBS@C was the calcined product of diatoms cultured in conventional medium without -SH.

Materials characterization

The crystalline structure of the samples was determined using a powder X-ray diffractometer (XRD, Rigaku SmartLab SE) at a scan step of 2°·min^{-1} with Cu Kα radiation. SEM (HITACHI SU8100) and transmission electron microscopy (TEM, TF20) were used to examine the morphology and microstructure of the samples. X-ray photoelectron spectroscopy (XPS, KRATOS, Axis UltraDLD) was performed, and the content of Ag$^+$ in the solution was determined using an inductively coupled plasma optical emission spectrometer (ICP-OES, SPECTRO BLUE). TG curves were measured using a thermogravimetric analyzer (PerkinElmer TL8000). The element content was measured and calculated by ICP-MS (Agilent 7800).

Half-cell assembly

The active materials (70 weight percent), carbon black (Super P, 20 weight percent), and polyvinylidene fluoride (PVDF, 10 weight percent) were mixed and dispersed in N-methyl-2-pyrrolidine (NMP), and the electrode slurry was obtained by ball milling at 300 rpm for 3 h. The slurry was cast on copper foil with a thickness of 50 m and dried in a vacuum oven at 80°C for 24 h. When the electrode sheets were dry, they were cut into 12 mm diameter sheets and used for cell assembly. The active material mass loading was 0.2–0.3 mg/cm^2. The electrolyte was 1 M LiPF$_6$ in a volume ratio of 1:1:1 EC/DEC/EMC. The counter and reference electrodes were made of lithium foil, and the separator was made of Celgard 2400. Finally, CR2016-type coin cells were assembled in an Ar-filled glove box.

Electrochemical performance testing

Galvanostatic charge-discharge tests were performed on a multichannel battery testing system (LAND CT3002A) with a constant current of 100–2000 mA g^{-1} in the potential range of 0.001–3.0 V (vs. Li/Li$^+$). An electrochemical workstation (Gamry Interface 1010E) was used to test cyclic voltammetry (CV) at a potential range of 0.01–3.0 V (vs. Li/Li$^+$) with a scan rate of 0.1 mV s^{-1} and electrochemical impedance spectroscopy (EIS) in a frequency range of 1 MHz–10 MHz.

QUANTIFICATION AND STATISTICAL ANALYSIS

The measurement of the Ag:Si molar ratio was performed using three replicate dataset and the standard deviation was calculated using Microsoft excel.